Catalysis Science & Technology

ROYAL SOCIETY OF CHEMISTRY

PAPER

View Article Online
View Journal | View Issue

Check for updates

Cite this: *Catal. Sci. Technol.*, 2026, **16**, 560

Received 11th July 2025,
Accepted 14th November 2025

DOI: 10.1039/d5cy00847f

rsc.li/catalysis

A comparative study of the effect of metal–support interaction on catalytic CO_2 methanation over Ni/$Ce_xZr_{1-x}O_2$ catalysts under thermal and plasma conditions

Yao Zhang, [ab] Huaizhong Xiang, [bc] Boji Wang, [b] Zhipeng Qie, [bd] Keran Jiao, [b]
Xuzhao Liu, [f] Xiaolei Fan *[be] and Shanshan Xu *[bf]

Metal–support interaction (MSI) is a well-established strategy for tuning catalytic activity in thermal catalysis, yet its role in nonthermal plasma catalytic CO_2 methanation remains insufficiently explored. In this study, Ni/$Ce_xZr_{1-x}O_2$ catalysts were synthesized using $Ce_xZr_{1-x}O_2$ supports calcined at different temperatures to systematically modulate the MSI. A volcano-shaped correlation was observed between the catalytic activity and support calcination temperature in both thermal and plasma systems. The $Ce_xZr_{1-x}O_2$ support calcined at 600 °C having a moderate particle size, demonstrated the optimum MSI (*i.e.*, promoting the facile formation of oxygen vacancies and stable interfacial anchoring of Ni particles) and thus the comparatively best catalytic performance under both conditions. Under the tested conditions, thermal CO_2 methanation exhibited superior activity compared to plasma-assisted reactions, *e.g.*, the NCZ-600 catalyst achieved an 83% CH_4 yield at 350 °C *versus* 11.3% at 7.0 kV. These results underscore the critical role of the MSI in governing CO_2 methanation across distinct catalytic environments and highlight its potential as a unifying design principle for both thermal and plasma catalysis.

1. Introduction

Carbon dioxide (CO_2) methanation is a key process for advancing the power-to-gas platform and enabling a circular carbon economy.[1] Due to its exothermic nature ($\Delta H°$ at 298 K $= -164$ kJ mol^{-1}), CO_2 methanation is thermodynamically favorable at relatively low temperatures (<400 °C).[2] However, at temperatures below ~200 °C, the reaction becomes kinetically limited, resulting in sluggish rates and a propensity for carbon deposition on the catalyst surface, which leads to deactivation. Thus, the practical implementation of CO_2 methanation system requires a delicate balance between thermodynamic favorability and kinetic accessibility. Catalyst design offers an effective strategy to overcome these limitations by lowering the activation energy, thereby enabling efficient methanation at reduced temperatures. Among the various approaches, tuning metal–support interaction (MSI) has been demonstrated to be an effective one to promote CO_2 methanation.

MSI refers to the electronic and structural interactions occurring at the metal–oxide interface, which strongly influence catalyst activity, selectivity, and stability. These effects arise from thermodynamic driving forces that lead to electron redistribution between the metal and the oxide support to achieve electronic equilibrium, as well as from atomic migration that stabilizes surface structures such as overlayers or alloys.[3] The phenomenon was first reported in 1978 by Tauster and co-workers,[4] who observed suppressed CO and H_2 chemisorption on group VIII metals supported on TiO_2 following high-temperature reduction. They attributed this to a strong chemical interaction at the interface, later termed metal–support interaction (MSI). Subsequent studies revealed that similar interactions in reducible oxide-supported noble and transition metal catalysts could substantially alter catalytic performance, often *via* encapsulation of metal nanoparticles by partially reduced oxide species.[5] In CO_2 hydrogenation, it has been shown to regulate both conversion and product selectivity. An optimally tuned MSI can minimize surface energy, prevent

---

[a] *School of Civil Engineering, Weifang University of Science and Technology, Weifang 262700, China*
[b] *Department of Chemical Engineering, The University of Manchester, Oxford Road, Manchester M13 9PL, UK*
[c] *Department of Chemistry, Queen Mary University of London, London E1 4NS, UK*
[d] *College of Mechanical and Energy Engineering, Beijing University of Technology, Beijing 100124, China*
[e] *Wenzhou Key Laboratory of Novel Optoelectronic and Nano Materials, Institute of Wenzhou, Zhejiang University, Wenzhou 325006, China*
[f] *Department of Materials, The University of Manchester, Oxford Road, Manchester M13 9PL, UK. E-mail: shanshan.xu@manchester.ac.uk*

nanoparticle aggregation, and thus enhance the adsorption and activation of intermediates (*e.g.*, CO), thereby promoting further hydrogenation to methane.[6–8] However, an excessively strong MSI may lead to over-encapsulation of active metal sites by the support, impeding reactant access and diminishing catalytic activity.[6] Thus, carefully balancing the beneficial stabilization effects of the MSI against the risks of over-encapsulation is crucial for maximizing CO_2 methanation efficiency and selectivity.

The conventional approach of modulating catalyst reduction temperature presents a fundamental trade-off. On the one hand, lowering the reduction temperature during catalyst preparation can partially alleviate over-encapsulation of active sites; on the other hand, it often results in insufficient electronic transfer and poor stabilization of metal nanoparticles.[9–11] This strategy is typically effective only for precious metals, which are readily reduced at low temperatures, but it offers limited benefits for widely used transition metals such as nickel (Ni), the preferred choice for selective CO_2 hydrogenation to methane.[9] To address this limitation, an alternative strategy is to adjust the calcination temperature of the catalyst support prior to metal loading. This simple yet powerful approach allows systematic tuning of key support properties, such as morphology, crystallinity, and surface chemistry,[12,13] thereby optimizing the MSI during subsequent metal deposition. Crucially, this method can enhance catalyst stability and activity while minimizing the risk of over-encapsulation.

In addition to catalyst design, nonthermal plasma (NTP) activation is another effective strategy for enabling CO_2 methanation under mild conditions. NTP catalytic systems operate under ambient temperature and atmospheric pressure, while the energetic electrons in plasma typically possess energies of 1–10 eV, sufficient to activate the highly stable CO_2 molecule.[14–16] Consequently, compared with conventional thermal catalytic systems, NTP catalytic CO_2 methanation can, in principle, achieve effective activation under significantly milder conditions. However, catalyst design strategies tailored specifically for NTP catalysis remain underexplored. For example, while tuning the metal–support interaction (MSI) is a well-established strategy in thermal catalysis, its applicability to NTP-assisted CO_2 methanation has received limited attention.[17] Considering the complex nature of plasma systems, where energetic electrons interact with ionized gases to generate a variety of reactive species such as radicals and ions, facilitating bond cleavage and formation, the role of the MSI in NTP systems may differ significantly from that in thermal catalysis.[16] Therefore, the feasibility of applying MSI-based catalyst design in NTP-assisted CO_2 methanation requires careful evaluation. Several pioneering studies have demonstrated the potential of this approach. For example, Sun *et al.* found that a plasma catalytic system using Pd/ZnO achieved nearly 36.7% CO_2 conversion and 35.5% CO yield, significantly outperforming plasma-only or plasma + ZnO systems. This enhancement was attributed to ZnO_x overlayers generated through strong MSI at the Pd–ZnO interface, combined with abundant hydrogen species on the Pd/ZnO surface.[18] Similarly, our recent work demonstrated that modulating the MSI in Ru/ZrO_2 catalysts, by tuning the ZrO_2 phase composition, influenced CO_2 hydrogenation under plasma conditions. Ru supported on mixed-phase ZrO_2 achieved 81.3% CO_2 conversion with 97.3% CH_4 selectivity, whereas Ru on monoclinic or tetragonal ZrO_2 promoted CO formation (>90%) with limited CO_2 conversion (<14%).[19] Despite these advances, comparative studies that systematically probe the influence of MSI on CO_2 methanation under both thermal and NTP conditions are scarce, and the underlying mechanisms of such design strategies remain poorly understood.

In this study, we proposed a simple method (*i.e.*, varying calcination temperature of the $Ce_xZr_{1-x}O_2$ support, CZ) to tune the particle size of the CZ support and thereby regulate the MSI in the resulting Ni/$Ce_xZr_{1-x}O_2$ (NCZ) catalysts. We systematically evaluated the catalytic performance of these NCZ catalysts for CO_2 methanation under both thermal and plasma conditions and correlated activity with structural and electronic properties. Among the series, the CZ support calcined at 600 °C (CZ-600) afforded the most favorable MSI, enabling stable anchoring of Ni particles and promoting oxygen vacancy formation, which facilitated CO_2 adsorption and activation. As a result, NCZ-600 delivered the best catalytic performance in both thermal and NTP systems. Notably, while thermal catalysis achieved higher CH_4 yields than NTP under the conditions studied, our results highlight the central role of the MSI in governing catalyst performance across both environments and point to additional factors unique to plasma catalysis that warrant further investigation.

2. Experimental

2.1. Chemicals

Unless otherwise stated, all chemicals and solvents, including zirconyl chloride octahydrate ($ZrOCl_2\cdot 8H_2O$, >98%), cerium(III) nitrate hexahydrate ($Ce(NO_3)_3\cdot 6H_2O$, >99%), nickel(II) nitrate hexahydrate ($Ni(NO_3)_2\cdot 6H_2O$, ≥98.5%) and ammonium hydroxide solution, (NH_4OH, 28.0–30.0% NH_3 basis), were purchased from Sigma-Aldrich and used as received without further purification.

2.2. Catalyst preparation

The $Ce_xZr_{1-x}O_2$ support was prepared by a modified co-precipitation method with a nominal composition of 60 mol% CeO_2 and 40 mol% ZrO_2.[20] In detail, stoichiometric quantities of $ZrOCl_2\cdot 8H_2O$ (1.07 g) and $Ce(NO_3)_3\cdot 6H_2O$ (2.17 g) were dissolved in deionized water. Then, an aqueous 28.0–30.0% ammonium hydroxide solution was added dropwise into the mixture at 80 °C under magnetic stirring to adjust the mixture pH value to about 10. Afterwards, the resulting mixture was digested at 80 °C for 24 h, washed thoroughly with deionized water and dried at 100 °C overnight. The obtained $Ce_xZr_{1-x}O_2$ support was calcined in an air flow at

500 °C, 600 °C, 700 °C, 800 °C or 900 °C, respectively, to attain the final $Ce_xZr_{1-x}O_2$-*T* (CZ-*T*) supports (where *T* represents the calcination temperature). The Ni supported on CZ-*T* catalysts (denoted as NCZ-*T*) were prepared *via* a conventional wet impregnation approach with a fixed theoretical Ni loading at 15 wt%. Specifically, 1.49 g of $Ni(NO_3)_2 \cdot 6H_2O$ and 2 g of the CZ-*T* support were dissolved in 30 mL deionized water. The suspension was mixed at room temperature for 1 h and, then the water was removed at 80 °C *via* evaporation. The obtained samples were calcined in flowing air at 500 °C for 4 h.

2.3. Catalyst characterization

The crystalline structure of the materials was determined by X-ray diffraction (XRD) using a Bruker diffractometer (D8 advance), with monochromatic Cu-Kα (λ = 1.5418 Å) as the radiation source. The 2θ range was 20 to 80° with a scan speed of 0.02° s^{-1} and a step size of 0.033°. Nitrogen adsorption analysis was conducted using a Micromeritics ASAP 2020 physisorption system at the liquid nitrogen temperature of −196 °C. The specific surface area of the materials (S_{BET}) was calculated using the Brunauer–Emmett–Teller (BET) method. X-ray photoelectron spectroscopy (XPS) measurements were performed using a Kratos AXIS Ultra Hybrid spectrometer (UK), which is equipped with a monochromatic Al Kα X-ray source. All spectra were calibrated to the C 1s peaks at a binding energy (B.E.) of 284.8 eV and fitted using XPSPEAK41 software. The Raman spectra were collected on a Renishaw inVia Raman spectrometer equipped with an argon ion laser with the emission line at 514 nm. The experiments were conducted with the acquisition time of 5 s, laser power of 7.5 mW, spectral resolution of 1 cm^{-1}, and ~1 μm laser spot size. The actual Ni loading of all reduced NCZ-*T* catalysts was measured using an inductively coupled plasma optical emission spectrometer (ICP-OES) (Varian 710-ES). About 20 mg of catalysts were digested in a mixed solution of hydrofluoric acid and *aqua regia* (with the ratio of $HCl : HNO_3 : HF$ is 1 : 3 : 1) *via* the method of microwave digestion (ETHOS UP microwave digester). The hydrogen temperature-programmed reduction (H_2-TPR) and CO_2 temperature-programmed desorption (CO_2-TPD) were performed on a Belcat II (Microtrac MRB, Japan) instrument. For H_2-TPR, ~50 mg of the calcined sample was reduced in 5% H_2/Ar gas flow at 10 °C min^{-1} from 200 to 800 °C. For CO_2-TPD, ~50 mg of the calcined catalysts were reduced *in situ* at 500 °C in 10% H_2/Ar and cooled down to 60 °C. CO_2 gas flow with the flowrate of 30 mL min^{-1} was purged for 1 h with the aim of adsorption. The physically adsorbed CO_2 was then removed by purging He for 1 h (at a flow rate of 30 mL min^{-1}). A mass spectrometer (MS, Hiden™ HPR-20) was used to analyze the effluent gas as the temperature increased from 60 to 800 °C with a ramping rate of 30 mL min^{-1}. The morphology of reduced NCZ catalysts and size of CZ supports were obtained by high-resolution transmission electron microscopy (HRTEM) at 300 kV on a Tecnai F30 (FEI, Germany) electron microscope equipped with a cold field emission gun (FEG) source. The scanning transmission electron microscope (STEM) and energy-dispersive X-ray spectroscopy (EDX) mapping images were obtained with a Titan STEM (G2 80-200), equipped with a high angle angular dark field (HAADF) detector. Each powder sample was dissolved and dispersed in ethanol and then drop-casted on a 300-mesh holey carbon grid prior to imaging.

2.4. Catalytic CO_2 methanation under thermal and plasma conditions

Thermal catalytic CO_2 methanation was conducted in a continuous fixed bed quartz reactor (Fig. S1). About 200 mg catalysts (355–500 μm) were reduced *in situ* in a 10% H_2/Ar gas flow for 2 h at 500 °C (10 °C min^{-1}) and a flow rate of 100 mL min^{-1} prior to the catalysis. A gas mixture of H_2/CO_2 (molar ratio of 4 : 1) balanced with Ar at a constant weight hourly space velocity (WHSV) of 30 000 mL (STP) $g_{cat}{}^{-1}$ h^{-1} was used for the reaction. The activity tests were carried out at between 100 and 500 °C with an interval of 50 °C. The composition of the outlet gas was monitored on-line by MS (Hiden™ HPR-20).

NTP-catalytic CO_2 methanation was carried out in a dielectric barrier discharge (DBD) plasma reactor (Fig. S2). Details of the NTP reactor system are described elsewhere.[2] The catalysts were all reduced under the same conditions above. However, due to the sample exposition to air, the reduced catalysts (~200 mg of pelletized catalysts, 355–500 μm) were treated again *in situ* by reducing plasma discharge (in H_2 balanced by Ar flow) at 6.5 kV for 0.5 h. Subsequently, a CO_2/H_2 gas flow with a molar ratio of 1 : 4 diluted in Ar was introduced into the NTP reactor for the reaction at a WHSV of 30 000 mL (STP) $g_{cat}{}^{-1}$ h^{-1}. The applied voltage adopted a range of 5.5–7.0 kV with a constant frequency of 20.5 kHz.

The CO_2 conversion (X_{CO_2}), selectivity to CH_4 (S_{CH_4}) and CO (S_{CO}), yield of CH_4 (Y_{CH_4}) and carbon balance ($C_{balance}$) are defined based on eqn (1)–(5):

$$X_{CO_2} = \frac{CO_{2,in} - CO_{2,out}}{CO_{2,in}} \times 100\% \quad (1)$$

$$S_{CH_4} = \frac{CH_{4,in}}{CO_{2,in} - CO_{2,out}} \times 100\% \quad (2)$$

$$S_{CO} = \frac{CO_{out}}{CO_{2,in} - CO_{2,out}} \times 100\% \quad (3)$$

$$Y_{CH_4} = X_{CO_2} \times S_{CH_4} \quad (4)$$

$$C_{balance}\,(\%) = \frac{CH_{4,out} + CO_{out} + CO_{2,out}}{CO_{2,in}} \quad (5)$$

For the thermal process, the apparent activation energy ($E_{a,thermal}$, kJ mol^{-1}) was determined using the Arrhenius equation (eqn (6)):

Table 1 Physical properties of the CZ-*T* supports

Sample	$d_{\text{support}}{}^{a}$ (nm)	Lattice parameter^{b} (Å) c
CZ-500	12.9	5.27410
CZ-600	13.8	5.27324
CZ-700	15.5	5.27291
CZ-800	17.4	5.27150
CZ-900	20.2	5.27127

[a] Average diameter of supports, estimated using TEM images. [b] Determined by XRD.

$$r_{\text{thermal}} = A \times \mathrm{e}^{-\frac{E_{\text{a,thermal}}}{RT}} \tag{6}$$

where A is the pre-exponential factor, R is the universal gas constant, and T is the reaction temperature (K).

For plasma catalysis, the apparent energy barrier ($E_{\text{a,NTP}}$, kJ mol^{-1}) was estimated following the approach reported in the literature, as shown in eqn (7):[21]

$$r_{\text{NTP}} = A \times \mathrm{e}^{\frac{E_{\text{a,NTP}}}{\frac{1}{F_{\text{total}}} \times \text{power}_{\text{DBD}}}} \tag{7}$$

where F_{total} is the total flow rate of feed gas, and power$_{\text{DBD}}$ is the DBD discharge power (W), calculated from the voltage–current characteristics recorded with a digital oscilloscope.

Using these methods, we determined the apparent activation energies of the catalysts under both thermal and plasma conditions (Fig. S5 and Table S1).

3. Results and discussion

3.1. Support size-dependent CO_2 methanation activity under thermal and NTP conditions

As summarized in Table 1, increasing the calcination temperature of the CZ-*T* supports from 500 °C to 900 °C led to a progressive increase in the support size (12.9–20.2 nm) and, after reduction, to larger metallic Ni particles (from 4.1 nm for NCZ-500 to 9.8 nm for NCZ-900). Classical structure–activity relationships suggest that smaller metal nanoparticles, with higher surface areas, typically enhance catalytic activity by exposing more active sites.[22] However, in this study, NCZ-500, which had the smallest Ni particle size (~4.1 nm) and support size (~12.9 nm), exhibited relatively low CH_4 yields (*e.g.*, less than 73.1% under thermal conditions and 9.1% under plasma conditions, Fig. S3). In contrast, NCZ-600, featuring an intermediate support size (~13.8 nm) and Ni particle size (~6.7 nm), achieved the highest CO_2 conversion and CH_4 yields under both thermal (*e.g.*, 95% and 83.0% at 350 °C) and plasma (*e.g.*, 15% and 11.3% at 7.0 kV) conditions (Fig. S3). Specifically, under thermal conditions, all the catalysts followed a volcano-shaped dependence of CO_2 conversion and CH_4 yield on the reaction temperature, with the activity peaking around 350 °C. At higher reaction temperatures (>350 °C), activity declined, consistent with thermodynamic limitations.[23] The performance order was NCZ-900 < NCZ-800 < NCZ-500 < NCZ-700 < NCZ-600 (Fig. 1 and S3a and c). NCZ-900 exhibited the lowest CH_4 yield, likely due to sintering and surface area loss at high calcination temperatures (Table 2). By contrast, under plasma conditions, CO_2 conversion and CH_4 yield increased monotonically with applied voltage, and the activity trend across catalysts was similar to the thermal case (*i.e.*, NCZ-900 < NCZ-800 < NCZ-700 < NCZ-500 < NCZ-600, Fig. S3b and d). Nevertheless, the absolute activity under plasma remained significantly lower than under thermal catalysis, particularly at temperatures above 250 °C. For example, NCZ-600 achieved a high CO_2 conversion of 90.3% and CH_4 yield of 81.3% at 300 °C. In contrast, under plasma conditions, the same catalyst exhibits a maximum CO_2 conversion of 15% and CH_4 yield of 11.3% at 7.0 kV at an

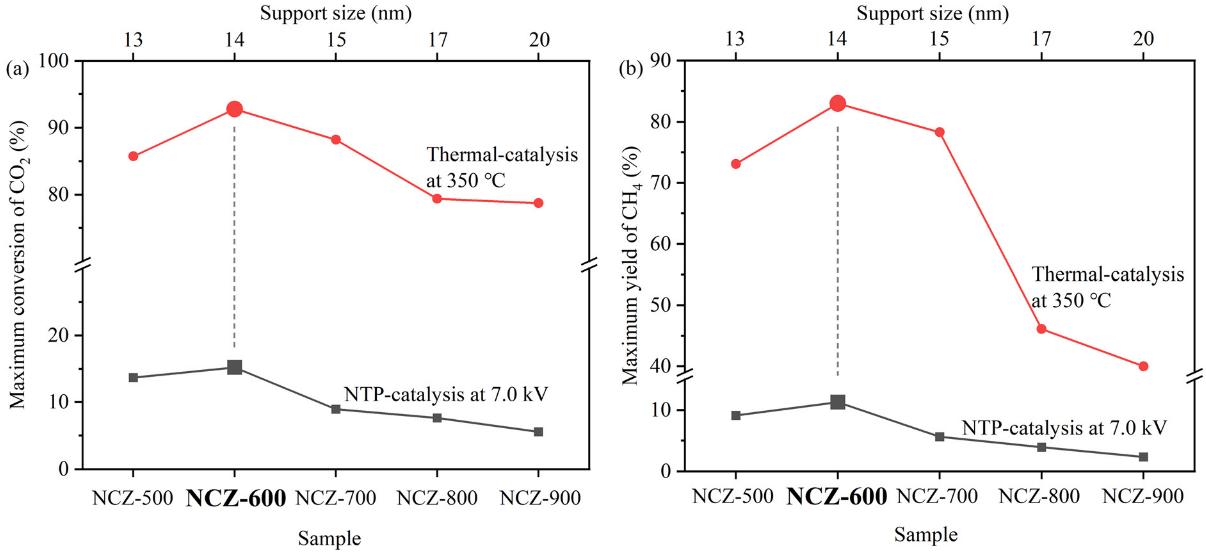

Fig. 1 Comparison of maximum (a) CO_2 conversion and (b) CH_4 yield under thermal conditions (at 350 °C) and NTP conditions (at 7.0 kV) over reduced NCZ-*T* catalysts with supports calcined at different temperatures.

Table 2 Relevant physicochemical properties of the reduced NCZ-*T* catalysts

		N_2 physisorption				Dimension			XPS analysis	
Catalyst	Ni[a] (wt%)	S_{BET}[b] ($m^2\ g^{-1}$)	V_p[b] ($cm^3\ g^{-1}$)	D_p[b] (nm)	d_{Ni}[c] (nm)	d_{Ni}[d] (nm)	d_{NiO}[e] (nm)	$D_{support}$[f] (nm)	$Ce^{3+}/(Ce^{3+} + Ce^{4+})$[g] (%)	$O_{surface}/(O_{lattice} + O_{surface} + O_{others})$[h] (%)
NCZ-500	15.2	30	0.066	8.4	4.1	4.1	3.6	15.1	27	46.5
NCZ-600	15	22	0.065	10.3	4.8	6.7	3.6	13.8	24.1	50.7
NCZ-700	14.9	21	0.065	12.5	6.6	7.2	3.8	17.2	26.2	43.9
NCZ-800	15	18	0.064	14.1	7.3	8.2	3.9	18.9	20	40.7
NCZ-900	15	10	0.051	18.8	7.9	9.8	3.8	24.8	17.4	36.2

[a] Determined by ICP-OES. [b] By N_2 physisorption. [c] Average particle size of Ni on the reduced NCZ-*T* catalysts calculated by the Debye–Scherrer equation based on XRD patterns. [d] Average particle size of Ni on the reduced catalysts from HRTEM images (Fig. 2). [e] Average particle size of NiO on the calcined NCZ-*T* catalysts based on XRD results. [f] Average support size of the reduced NCZ-*T* catalysts, obtained from TEM images (Fig. S4). [g] Extracted from the deconvoluted Ce 3d XPS spectra. [h] Estimated oxygen vacancy concentration from O 1s XPS spectra.

applied voltage of 7.0 kV (Fig. S3). The performance gap between the two systems was reflected mainly by methane selectivity (Fig. S4). For example, nearly 100% CH_4 selectivity is achieved by NCZ-600 at 200 °C in the thermal system, whereas only 70% selectivity is observed at 7 kV under plasma conditions (Fig. S4). Interestingly, the NCZ-600 catalyst exhibited relatively high activation energy (*i.e.*, 96.14 kJ mol^{-1} in the NTP system and 84.06 kJ mol^{-1} in the thermal system, Fig. S5 and Table S1) yet delivered the best overall performance compared to other catalysts. All catalysts in the plasma system displayed higher activation energies than those in the thermal system, suggesting that MSI modulation may alter the reaction kinetics. Plasma catalysis, however, is governed by a distinct set of kinetic constraints. These include (i) energy-transfer kinetics, where the energy efficiency depends on matching the electron energy distribution with molecular excitation cross-sections;[24] (ii) surface-reaction kinetics, as plasma-generated reactive species may quench upon collision with the catalyst surface;[16] (iii) transport kinetics of short-lived reactive species, whose limited lifetimes restrict their effective interaction with surface active sites.[16] The observed higher activation energy can be rationalized by the isokinetic relationship: lower activation energy enhances the activity only in the region $T < T_i$ (isokinetic point), whereas in the region $T > T_i$, higher activation energy can benefit more active catalysts. The kinetic study therefore points to possible alternative pathways in plasma-assisted CO_2 methanation reactions.[25] The kinetic study therefore points to possible alternative pathways in plasma-assisted CO_2 methanation reactions. Comparison with reported activity data in the literature (Table S3) shows that the NCZ-600 catalyst delivers a significantly higher methane yield, outperforming many state-of-the-art thermal and NTP catalytic systems.

The volcano-shaped activity trend observed with respect to the support calcination temperature is likely attributed to changes in the support size rather than the Ni particle size (Fig. 1 and S8 and Table 2). Specifically, similar average NiO particle sizes (~3.6–3.9 nm) across all calcined NCZ-*T* samples were observed. However, after reduction at 500 °C, the metallic Ni particle size increases significantly from ~4.1 nm in NCZ-500 to ~9.8 nm in NCZ-900 (Table 2, Fig. 2, S6

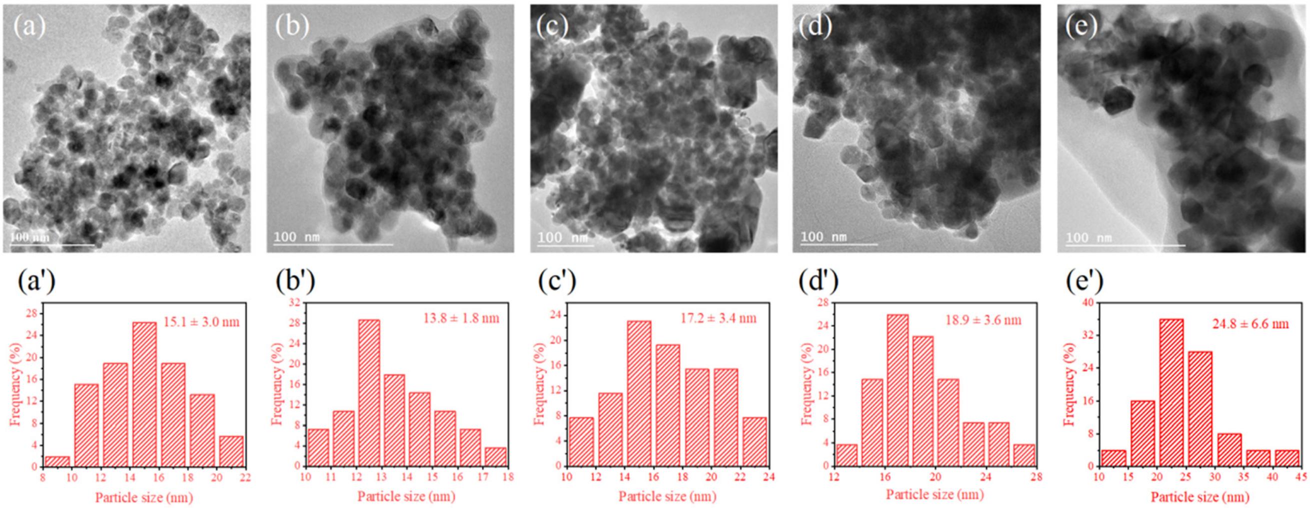

Fig. 2 TEM images and corresponding support size of the reduced (a and a′) NCZ-500 (b and b′) NCZ-600 (c and c′) NCZ-700 (d and d′) NCZ-800 and (e and e′) NCZ-900 catalysts (reduced at 500 °C).

and S8). Interestingly, the NCZ-500 catalyst, which has the smallest Ni particle size (*i.e.*, the highest metal surface area), does not show favorable CO_2 methanation activity, indicating that the Ni particle size is not the primary factor to affect the catalyst performance.[26] Instead, NCZ-600 with an optimal support structure, which demonstrates the highest activity, does not exhibit the smallest Ni particles or the largest Ni surface area. This suggests that the enhanced catalytic performance of the NCZ-600 catalyst is primarily attributed to the strength of the metal–support interaction between Ni nanoparticles and CZ-*T* supports, rather than Ni particle size effects.

3.2. Influence of the MSI on the catalyst properties and catalytic performance

3.2.1 Stable interfacial anchoring Ni on the CZ-600 support. The volcano-shaped catalytic activity trend observed for NCZ-*T* catalysts as a function of support calcination temperature can be rationalized by differences in the strength of the MSI. Modulating the MSI plays a critical role in stabilizing Ni species on the support surface, thereby influencing catalytic performance. Transmission electron microscopy (TEM) analysis confirmed that an optimal level of MSI contributes to catalyst stability, even under harsh reduction conditions.

After reduction at 500 °C, metallic Ni particle sizes increased progressively from ~4.1 to 9.8 nm across the catalyst series, as determined by both STEM and XRD (Fig. S8), suggesting Ni sintering/agglomeration at higher calcination temperatures. This agglomeration is likely a consequence of the decreased surface area of the CZ supports at elevated calcination temperatures (*e.g.*, S_{BET} = 10 m^2 g^{-1} for NCZ-900, Table 2). Interestingly, TEM results (Tables 1 and 2) show that the NCZ-600 catalyst retained a support size (~13.8 nm) comparable to that of the parent CZ-600 support after reduction. Conversely, other catalysts exhibited a pronounced increase in the support size after reduction (Fig. S9 and 2). This finding suggests that NCZ-600, possessing an intermediate support size, offers an optimal balance of MSI and thermal stability, effectively suppressing support surface area loss during high-temperature treatment. Such stabilization minimizes Ni sintering and preserves active interfacial sites, which accounts for the superior catalytic activity of NCZ-600 under both thermal and plasma conditions.

In addition to providing stable anchoring sites for Ni species, modulation of the MSI also influences the reductivity of Ni species on the support. To investigate this, temperature-programmed reduction with hydrogen (H_2-TPR) experiments were conducted. As shown in Fig. 3, four reduction peaks were observed for all catalysts. The lowest-temperature peak (α), appearing below ~300 °C, corresponds to the removal of surface adsorbates or the reduction of easily reducible surface Ni^{2+} species. The highest-temperature small peak, above ~700 °C, is attributed to the bulk reduction of Ce^{4+} species, which is relatively unaffected by the presence of Zr or Ni species.[27] The dominant peak β, centered around ~366 °C, can be ascribed to the reduction of bulk or subsurface Ni^{2+} species. Additionally, a smaller shoulder peak γ (~410–453 °C) is associated with the reduction of Ce^{4+} to Ce^{3+} within the distorted fluorite

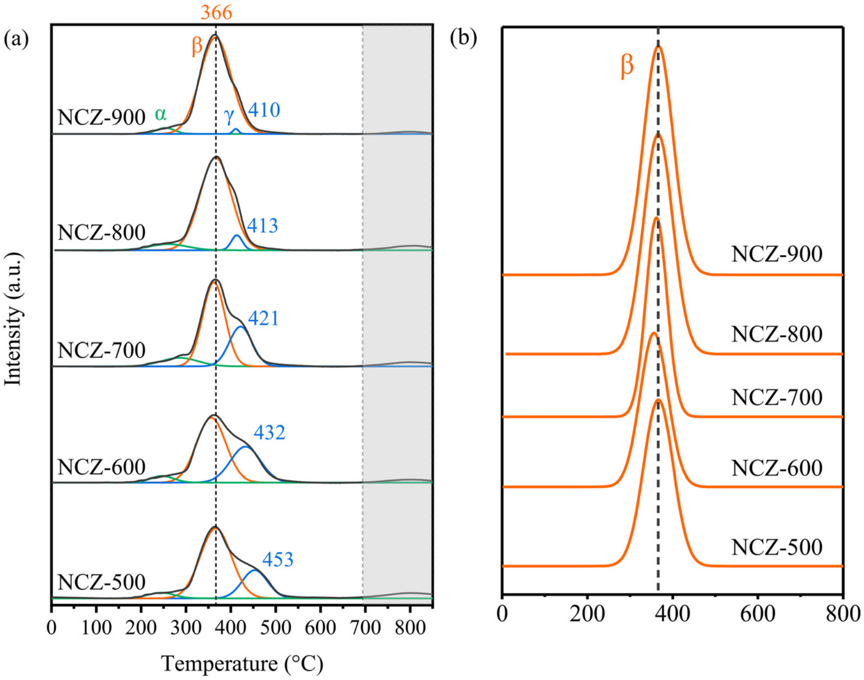

Fig. 3 (a) H_2-TPR profiles and (b) enlarged deconvoluted peak β of the calcined NCZ-*T* catalysts.

structure, accompanied by the formation of oxygen vacancies, and is influenced by the presence of dispersed Ce^{4+} and Ni^{2+} ions.[27,28]

For NCZ-600, the Ni^{2+} reduction peak (β) appears at a slightly lower temperature (∼356 °C) compared with other catalysts, before shifting progressively to higher temperatures as the support calcination temperature increases to 900 °C. This behavior suggests that NCZ-600 exhibits the weakest MSI within the series, facilitating Ni^{2+} reduction. By contrast, the decreased CO_2 methanation activity of NCZ-800 and NCZ-900 is likely due to the stronger MSI, which encouraged the formation of a thicker support overlayer over the Ni particles.[29] Meanwhile, the γ peak displays a systematic shift toward lower temperatures (from 453 °C to 410 °C) with increasing support calcination temperature (500 °C to 900 °C), reflecting enhanced reducibility of Ce^{4+} in the distorted fluorite structure. Notably, H_2 consumption for the γ peak reaches its maximum in NCZ-600, indicating the highest concentration of oxygen vacancies achieved after calcination at 600 °C. After calcination at higher temperatures (≥700 °C), the γ peak decreases significantly, suggesting a reduced extent of Ce^{4+} to Ce^{3+} transformation and consequently fewer oxygen vacancies.

3.2.2 Facile formation of oxygen vacancies for enhanced CO_2 adsorption. To further investigate the role of the MSI in oxygen vacancy formation, X-ray diffraction (XRD) and Raman spectroscopy were employed to analyze the structural properties of CZ-*T* supports and NCZ-*T* catalysts. As shown in Fig. 4, the XRD patterns of all CZ-*T* supports and NCZ-*T* catalysts exhibit characteristic diffraction peaks at 28.5°, 47.5°, and 56.3°, corresponding to the (111), (220), and (311) planes of the cubic phase CeO_2 (PDF#43-1002). Additionally, the Ni and NiO phases are identified in the reduced and calcined samples, respectively. The lattice parameters of the CZ-*T* supports, listed in Table 1, are slightly lower than that of pure CeO_2 (5.41 Å, PDF#43-1002), suggesting the successful incorporation of Zr^{4+} into the Ce^{4+} lattice to form a $Ce_xZr_{1-x}O_2$ solid solution. This is attributed to the smaller ionic radius of Zr^{4+} (0.84 Å) compared to Ce^{4+} (0.97 Å).[30] Moreover, weak diffraction peaks corresponding to the tetragonal phase of ZrO_2 were detected in all samples and became more prominent at higher calcination temperatures, indicating

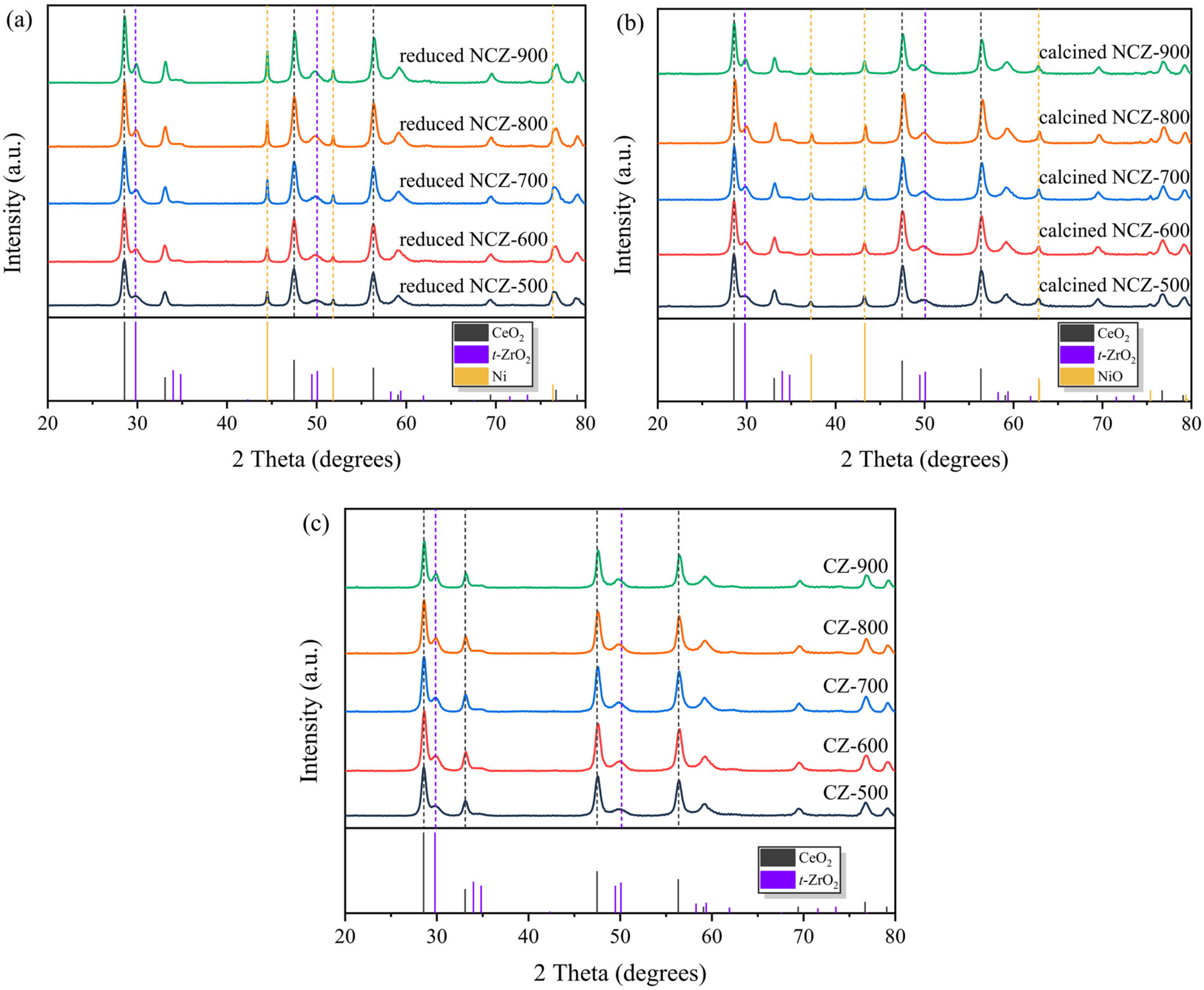

Fig. 4 XRD patterns of (a) the reduced NCZ-*T* catalysts, (b) the calcined NCZ-*T* samples and (c) the calcined CZ-*T* supports.

partial phase segregation at elevated temperatures. For the reduced catalysts, diffraction peaks at 44.5°, 51.8°, and 76.4° are assigned to the (111), (200), and (220) planes of metallic Ni (PDF#04-0850), respectively. Furthermore, after reduction, the increased intensity of both CeO_2 and Ni reflections with increasing calcination temperature suggests enhanced crystallinity and crystallite growth of both phases, implying that higher calcination temperatures promote greater crystallite growth prior to the reduction process.

Raman spectroscopy was subsequently employed to investigate the oxygen vacancy formation (Fig. 5a). The phase composition of the zirconia–ceria system can form distinct structural phases depending on the calcination temperature and the Zr/Ce ratio.[31] According to the literature, the strong broad band at 467 cm^{-1}, along with two weak bands at ∼260 cm^{-1} (E_g), and 315 cm^{-1} (B_{1g}), originates from the six active Raman modes of $A_{1g} + 2B_{1g} + 3E_g$ associated with the tetragonal ZrO_2 phase (space group *P*42/*nmc*), indicating the presence of a small amount of tetragonal ZrO_2 in the samples.[32,33] The prominent Raman peak at ∼467 cm^{-1}, observed in all samples, is attributed to the F_{2g} vibrational mode of the fluorite cubic structure of CeO_2 (symmetrical stretching of the Ce–O bonds), which is associated with the presence of oxygen vacancies. These vacancies are formed through the substitution of Ce^{4+} by Zr^{4+}, leading to the generation of a CeO_2–ZrO_2 solid solution in the CZ-*T* supports, which is consistent with the above XRD results. In the reduced NCZ-*T* catalysts, additional oxygen vacancies are introduced due to the partial reduction of Ce^{4+} to Ce^{3+} during the reduction process.[27,34] Furthermore, a broad and weak band at *ca.* 620 cm^{-1} in both CZ-*T* and NCZ-*T* samples, namely the defect-induced longitudinal optical band (*i.e.*, LO band), can be assigned to structural defects and oxygen vacancies within the fluorite lattice.[27,35]

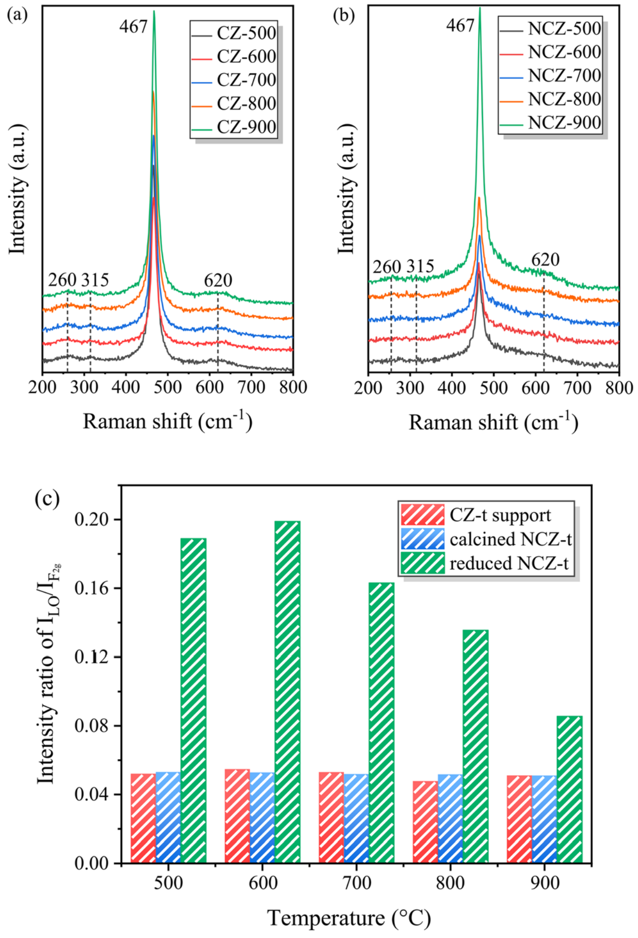

Fig. 5 Raman spectra for (a) the CZ-*T* supports and (b) the reduced NCZ-*T* catalysts and (c) the corresponding $I_{LO}/I_{F_{2g}}$ values.

The intensity ratio of the LO to the F_{2g} bands can be used as an indicator of the oxygen vacancy density.[27] As shown in Fig. 5(c), this ratio shows no significant variation among the CZ-*T* supports or the calcined NCZ-*T* samples, suggesting that the oxygen vacancy concentration remains relatively unchanged after calcination. Interestingly, after reduction treatment at 500 °C, the $I_{LO}/I_{F_{2g}}$ ratio for the reduced NCZ-*T* catalysts initially increased and then decreased, displaying a volcano-like trend with NCZ-600 showing the highest value of 0.20 (Fig. 5c). This suggests that the variation in oxygen vacancy density is not from the calcination of the supports or the loading of nickel species, but rather from the reduction process, specifically the partial reduction of Ce^{4+} to Ce^{3+} in the Ce_nO_{2n}-based lattice during catalyst activation.[36] The highest oxygen vacancy density observed in NCZ-600 can thus be attributed to an optimal MSI, where Ni nanoparticles interact with supports to promote partial reduction of Ce^{4+} to Ce^{3+}. This enhanced generation of Ce^{3+} leads to a higher concentration of oxygen vacancies, which in turn facilitates superior catalytic performance.

To further elucidate the MSI and its influence on the formation of oxygen vacancies, the surface characteristics of all NCZ-*T* catalysts were examined using X-ray photoelectron spectroscopy (XPS) analysis (Fig. S12a and 6). In the O 1s spectrum, the photoelectron peaks correspond to: (i) lattice oxygen ($O_{lattice}$) at ∼529.4 eV, (ii) surface oxygen species ($O_{surface}$: O^{2-}, O_2^{2-} or O^-) at ∼531.1 eV and (iii) weakly bound oxygen species such as CO_3^{2-}, hydroxyl groups and surface-adsorbed H_2O (O_{others}) at ∼533.0 eV.[37] As shown in Fig. 6 and Table 2, the concentration of oxygen vacancies, calculated as $O_{surface}/O_{lattice} + O_{surface} + O_{others}$, increased initially and then decreased again with increasing support calcination temperature, with maximum oxygen vacancy concentration achieved by NCZ-600, which is consistent with the results from H_2-TPR (γ peak) and Raman measurements ($I_{LO}/I_{F_{2g}}$).

This phenomenon is further supported by the Ce 3d XPS spectra, which display two sets of multiplets corresponding to the spin–orbit components $3d_{3/2}$ and $3d_{5/2}$. The deconvoluted peaks labeled v_0 (879.91 eV), v_2 (884.48 eV), u_0 (898.55 eV) and u_2 (902.84 eV) are assigned to the Ce $3d^{10}4f^1$ state of Ce^{3+}, while the peaks labeled v_1 (882 eV), v_3 (888.4 eV), v_4 (897.8 eV), u_1 (900.7 eV), u_3 (907.2 eV) and u_4 (917 eV) correspond to the Ce $3d^{10}4f^0$ state of Ce^{4+}.[27] A decreasing Ce signal is observed with increasing calcination temperature of the supports, indicating aggregation of Ce species in catalysts

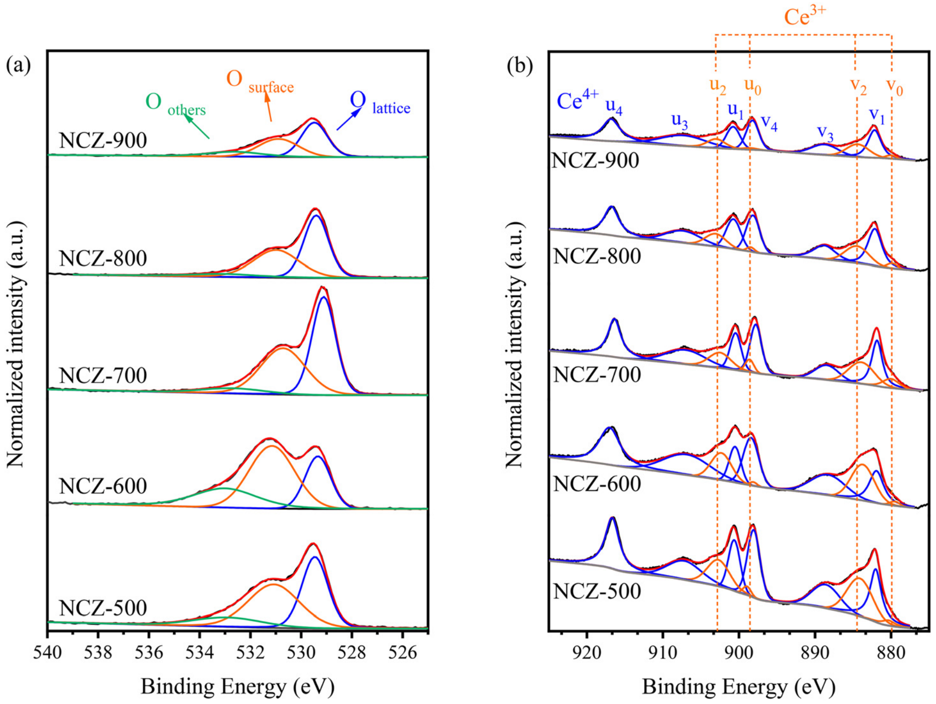

Fig. 6 XPS spectra of the reduced NCZ-*T* catalysts: (a) O 1s and (b) Ce 3d.

with supports calcined at higher temperatures (Fig. S12b and 6b). CeO_2 has the capacity to store and release oxygen through the redox reaction ($2CeO_2 \leftrightarrow Ce_2O_3 + 1/2O_2$), where each released oxygen atom creates an oxygen vacancy and simultaneously converts two Ce^{4+} ions to Ce^{3+} *via* electron transfer.[36] Thereby, the ratio of $Ce^{3+}/(Ce^{3+} + Ce^{4+})$ can be used to indicate the oxygen vacancy density. This ratio follows the same trend as the concentration of oxygen vacancies observed in the O 1s spectra, further confirming the consistency of the findings.

Based on above findings, we can conclude that the support calcination temperature of 600 °C, associated with weak metal support interaction, promotes the formation of oxygen vacancies. The facile generation of these vacancies is beneficial for CO_2 methanation, where the role of the support is critical.[38] The CZ-*T* supports are particularly effective in CO_2 adsorption and its activation at the interface, owing to their pronounced redox properties and abundant oxygen vacancies, which can readily interact with CO_2 molecules to generate reactive intermediates such as carboxylates during CO_2 methanation.[13,39] This enhancement in CO_2 adsorption due to oxygen defects is further supported by CO_2-TPD results (Fig. S13), where NCZ-600 shows moderate basic sites for CO_2 adsorption. In plasma-assisted systems, where plasma discharges can create new active sites, or reactivate adsorption sites, tuning the MSI may potentially enable new reaction pathways by modulating oxygen vacancy formation under plasma conditions.[40–42] This may also explain the comparatively lower catalytic activities observed in plasma environments than that of thermal catalysis when applying the same MSI-based strategy. Previous studies have shown that plasma-catalytic CO_2 methanation over supported Ni catalysts proceeds *via* similar pathways to thermal catalysis, that is, forming surface carbonate and/or formate intermediates, which are subsequently hydrogenated to methane.[41–43] The key difference in plasma-catalytic CO_2 methanation is the activation of reactant molecules in gas discharge by electron-impact dissociation and/or gas-phase reactions. For example, plasma can activate CO_2 and H_2 in the gas discharge to form reactive intermediates such as vibrationally excited CO_2, CO, and H species. These short-lived gas species can directly interact with catalyst surfaces and participate in the hydrogenation *via* Hinshelwood–Rideal mechanisms, forming a CO-hydro pathway for methane, as demonstrated by previous studies.[43,44]

The relevant post-plasma characterisation, including Raman and XRD analyses, was conducted to evaluate possible surface modifications and MSI changes (Fig. S10 and S11, Pages S9). As shown by XRD in Fig. S10, negligible changes were observed in the patterns of the used NCZ-*T* samples, and no NiO diffraction peaks were detected, confirming the absence of Ni oxidation and indicating similar Ni dispersions compared to the fresh catalyst under plasma discharge conditions. Raman results further revealed that the abundance of oxygen vacancies (reflected by $I_{LO}/I_{F_{2g}}$ values) in the used NCZ-*T* catalysts had the same volcano-type trend as in the reduced catalysts (with NCZ-600 showing the maximum concentration), suggesting that the MSI features of the catalysts under investigation were preserved after plasma catalysis. A slight overall increase in oxygen vacancy intensity was observed for all used catalysts, being similar to previous findings that plasma treatment can generate additional oxygen vacancies *via* oxygen atom removal from the CeO_2 surface.[45–47] Overall, these results suggest that plasma discharge does not cause significant changes on the Ni state and MSI during the plasma-catalytic reactions.

4. Conclusion

The improvement of CO_2 methanation requires careful alignment of catalyst design and operating conditions to simultaneously satisfy thermodynamic favorability and kinetic accessibility. In this work, a facile approach (tuning the support size *via* varying calcination temperature) was employed to regulate the MSI of Ni supported on $Ce_xZr_{1-x}O_2$ catalysts (Ni/CZ), and thereby the performance of catalytic CO_2 methanation under both thermal and plasma conditions. Comparative catalytic experiments revealed that the MSI exerts a similar influence on CO_2 methanation in both environments, following a volcano-shaped relationship between catalytic activity and support calcination temperature. This finding suggests that intrinsic catalytic activity, typically assessed under thermal conditions, can in part be transferred to plasma catalysis. Among the catalysts tested, NCZ-600 (prepared from CZ calcined at 600 °C) demonstrated the most favorable balance of properties, achieving CH_4 yields of 83% at 350 °C under thermal conditions and 11.3% at 7.0 kV under NTP conditions. Structural characterization confirmed that NCZ-600 possessed an intermediate support size (~13.8 nm), the highest concentration of oxygen vacancies, and stably anchored Ni species, together enabling superior performance in both catalytic systems. The observed differences in the activity between thermal and plasma catalysis highlight two important implications: (i) plasma catalytic systems must be further optimized to unlock the full potential of catalysts that perform well under thermal conditions, and/or (ii) bespoke catalyst design tailored specifically for plasma environments is required. Given the fundamentally different activation mechanisms, thermal activation *versus* plasma-induced energetic species, future efforts should focus on unraveling how plasma alters catalyst surfaces and reaction pathways. Addressing these questions will be crucial for advancing hybrid NTP catalytic technologies toward efficient and practical CO_2 conversion.

Conflicts of interest

There are no conflicts to declare.

Data availability

This is to confirm that all data supporting the findings of this study are included in the article and its supplementary information (SI). Additional raw data or experimental details can be obtained from the corresponding author upon request.

Supplementary information: the supplementary activity results, BET, STEM, XPS and characterisation of spent catalysts are included in the SI. See DOI: https://doi.org/10.1039/d5cy00847f.

Acknowledgements

The authors thank the special innovation fund from the Institute of Wenzhou, Zhejiang University (No. XMGL-KJZX-202204) for supporting the collaboration. This project has received funding from the European Union's Horizon 2020 research and innovation program under grant agreement No. 872102 and 101022507. This project is also supported by the Wenzhou Municipal Science and Technology (G20240011) for research collaboration. Y. Z. and B. W. thank the financial support from the China Scholarship Council (file no. 202006100040, 202106100037) and the University of Manchester (United Kingdom) for supporting their PhD research at the University of Manchester. This work was also supported by the Research Start-up Funding Project for High-level Talents of Weifang University of Science and Technology (KJRC2025029). TEM access at the University of Manchester was supported by the Henry Royce Institute for Advanced Materials, funded through EPSRC grants EP/R00661X/1, EP/S019367/1, EP/P025021/1 and EP/P025498/1.

References

1 C. H. Tan, *et al.*, Current Developments in Catalytic Methanation of Carbon Dioxide—A Review, *Front. Energy Res.*, 2022, **9**, 795423, DOI: 10.3389/fenrg.2021.795423.

2 Y. Zhang, *et al.*, Plasma-catalytic CO_2 methanation over $NiFe_n/(Mg, Al)O_x$ catalysts: Catalyst development and process optimisation, *Chem. Eng. J.*, 2023, **465**, 142855, DOI: 10.1016/j.cej.2023.142855.

3 D. Leybo, *et al.*, Metal-support interactions in metal oxide-supported atomic, cluster, and nanoparticle catalysis, *Chem. Soc. Rev.*, 2024, **53**, 10450–10490, DOI: 10.1039/d4cs00527a.

4 S. J. Tauster, S. C. Fung and R. L. Garten, Strong Metal-Support Interactions. Group 8 Noble Metals Supported on TiO_2, *J. Am. Chem. Soc.*, 1978, **100**(1), 170–175, DOI: 10.1021/ja00469a029.

5 W. Wang, X. Zhang, S. Weng and C. Peng, Tuning Catalytic Activity of CO_2 Hydrogenation to C1 Product via Metal Support Interaction Over Metal/Metal Oxide Supported Catalysts, *ChemSusChem*, 2024, **17**, 202400104, DOI: 10.1002/cssc.202400104.

6 T. Pu, W. Zhang and M. Zhu, Engineering Heterogeneous Catalysis with Strong Metal–Support Interactions: Characterization, Theory and Manipulation, *Angew. Chem., Int. Ed.*, 2023, **62**, e202212278, DOI: 10.1002/anie.202212278.

7 S. Li, *et al.*, Tuning the Selectivity of Catalytic Carbon Dioxide Hydrogenation over Iridium/Cerium Oxide Catalysts with a Strong Metal–Support Interaction, *Angew. Chem., Int. Ed.*, 2017, **56**, 10761–10765, DOI: 10.1002/anie.201705002.

8 J. Zhou, *et al.*, Interfacial compatibility critically controls Ru/TiO_2 metal-support interaction modes in CO_2 hydrogenation, *Nat. Commun.*, 2022, **13**, 327, DOI: 10.1038/s41467-021-27910-4.

9 S. Yuan, *et al.*, CO_2 methanation boosted by support-size-dependent strong metal-support interaction and B–O–Ti component, *Green Energy Environ.*, 2024, **9**, 321–332, DOI: 10.1016/j.gee.2022.05.010.

10 A. Corma, P. Serna, P. Concepción and J. J. Calvino, Transforming Nonselective into Chemoselective Metal Catalysts for the Hydrogenation of Substituted Nitroaromatics, *J. Am. Chem. Soc.*, 2008, **130**, 8748–8753, DOI: 10.1021/ja800959g.

11 H. Tang, *et al.*, Classical strong metal–support interactions between gold nanoparticles and titanium dioxide, *Sci. Adv.*, 2017, **3**, e1700231, DOI: 10.1126/sciadv.1700231.

12 J. Ren, *et al.*, Ni-based hydrotalcite-derived catalysts for enhanced CO2 methanation: Thermal tuning of the metal-support interaction, *Appl. Catal., B*, 2024, **340**, 123245, DOI: 10.1016/j.apcatb.2023.123245.

13 A. Parastaev, *et al.*, Boosting CO_2 hydrogenation via size-dependent metal–support interactions in cobalt/ceria-based catalysts, *Nat. Catal.*, 2020, **3**, 526–533, DOI: 10.1038/s41929-020-0459-4.

14 Y. Yi, *et al.*, Selective oxidation of CH_4 to CH_3OH through plasma catalysis: Insights from catalyst characterization and chemical kinetics modelling, *Appl. Catal., B*, 2021, **296**, 120384, DOI: 10.1016/j.apcatb.2021.120384.

15 R. Snoeckx and A. Bogaerts, Plasma technology – a novel solution for CO_2 conversion?, *Chem. Soc. Rev.*, 2017, **46**, 5805–5863, DOI: 10.1039/C6CS00066E.

16 E. C. Neyts, K. Ostrikov, M. K. Sunkara and A. Bogaerts, Plasma Catalysis: Synergistic Effects at the Nanoscale, *Chem. Rev.*, 2015, **115**, 13408–13446, DOI: 10.1021/acs.chemrev.5b00362.

17 P. Frontera, A. Macario, M. Ferraro and P. Antonucci, Supported Catalysts for CO_2 Methanation: A Review, *Catalysts*, 2017, **7**(2), 59.

18 Y. Sun, *et al.*, Plasma-Catalytic CO_2 Hydrogenation over a Pd/ZnO Catalyst: In Situ Probing of Gas-Phase and Surface Reactions, *JACS Au*, 2022, **2**, 1800–1810, DOI: 10.1021/jacsau.2c00028.

19 Y. Zhang, *et al.*, On understanding the effect of metal-support interactions on plasma-catalytic CO2 hydrogenation over the Ru/ZrO2 catalysts, *Chem. Eng. J.*, 2025, **518**, 164799.

20 S. Gopalakrishnan, *et al.*, Unravelling the structure and reactivity of supported Ni particles in Ni-$CeZrO_2$ catalysts, *Appl. Catal., B*, 2013, **138–139**, 353–361, DOI: 10.1016/j.apcatb.2013.02.036.

21 J. Kim, D. B. Go and J. C. Hicks, Synergistic effects of plasma–catalyst interactions for CH_4 activation, *Phys. Chem. Chem. Phys.*, 2017, **19**, 13010–13021, DOI: 10.1039/C7CP01322A.

22 P. Munnik, P. E. de Jongh and K. P. de Jong, Recent Developments in the Synthesis of Supported Catalysts, *Chem. Rev.*, 2015, **115**, 6687–6718, DOI: 10.1021/cr500486u.

23 B. Varandas, M. Oliveira, C. Andrade and A. Borges, Thermodynamic Equilibrium Analysis of CO_2 Methanation through Equilibrium Constants: A Comparative Simulation Study, *Physchem*, 2024, **4**, 258–271.

24 A. Fridman, *Plasma Chemistry*, Cambridge University Press, 2008.

25 H. Kral and W. Reschetilowski, A Reconsideration of the Conventional Rule in Catalysis and the Consequences, *Processes*, 2025, **13**, 917.

26 L. Li, *et al.*, Research Progress and Reaction Mechanism of CO_2 Methanation over Ni-Based Catalysts at Low Temperature: A Review, *Catalysts*, 2022, **12**(2), 244.

27 B. Safavinia, *et al.*, Enhancing $Ce_xZr_{1-x}O_2$ Activity for Methane Dry Reforming Using Subsurface Ni Dopants, *ACS Catal.*, 2020, **10**, 4070–4079, DOI: 10.1021/acscatal.0c00203.

28 Y. Yu, *et al.*, Influence of Calcination Temperature on Activity and Selectivity of Ni-CeO_2 and Ni-$Ce_{0.8}Zr_{0.2}O_2$ Catalysts for CO_2 Methanation, *Top. Catal.*, 2018, **61**, 1514–1527, DOI: 10.1007/s11244-018-1010-6.

29 L. Shen, J. Xu, M. Zhu and Y.-F. Han, Essential role of the support for nickel-based CO_2 methanation catalysts, *ACS Catal.*, 2020, **10**, 14581–14591.

30 M. Mikhail, *et al.*, Electrocatalytic behaviour of $CeZrO_x$-supported Ni catalysts in plasma assisted CO_2 methanation, *Catal. Sci. Technol.*, 2020, **10**, 4532–4543, DOI: 10.1039/D0CY00312C.

31 M. Yashima, H. Arashi, M. Kakihana and M. Yoshimura, Raman Scattering Study of Cubic-Tetragonal Phase Transition in $Zr_{1-x}Ce_xO_2$ Solid Solution, *J. Am. Ceram. Soc.*, 1994, **77**, 1067–1071, DOI: 10.1111/j.1151-2916.1994.tb07270.x.

32 E. Fernández López, V. Sánchez Escribano, M. Panizza, M. M. Carnasciali and G. Busca, Vibrational and electronic spectroscopic properties of zirconia powders, *J. Mater. Chem.*, 2001, **11**, 1891–1897, DOI: 10.1039/B100909P.

33 J. Li, *et al.*, Preparation of high oxygen storage capacity and thermally stable ceria–zirconia solid solution, *Catal. Sci. Technol.*, 2016, **6**, 897–907, DOI: 10.1039/C5CY01571E.

34 R. Si, Y.-W. Zhang, S.-J. Li, B.-X. Lin and C.-H. Yan, Urea-Based Hydrothermally Derived Homogeneous Nanostructured $Ce_{1-x}Zr_xO_2$ (x = 0-0.8) Solid Solutions: A Strong Correlation between Oxygen Storage Capacity and Lattice Strain, *J. Phys. Chem. B*, 2004, **108**, 12481–12488, DOI: 10.1021/jp048084b.

35 B. M. Reddy, *et al.*, Raman and X-ray Photoelectron Spectroscopy Study of CeO_2-ZrO_2 and V_2O_5/CeO_2-ZrO_2 Catalysts, *Langmuir*, 2003, **19**, 3025–3030, DOI: 10.1021/la0208528.

36 A. Migani, G. N. Vayssilov, S. T. Bromley, F. Illas and K. M. Neyman, Greatly facilitated oxygen vacancy formation in ceria nanocrystallites, *Chem. Commun.*, 2010, **46**, 5936–5938, DOI: 10.1039/C0CC01091J.

37 M. Asnavandi, Y. Yin, Y. Li, C. Sun and C. Zhao, Promoting Oxygen Evolution Reactions through Introduction of Oxygen Vacancies to Benchmark NiFe–OOH Catalysts, *ACS Energy Lett.*, 2018, **3**, 1515–1520, DOI: 10.1021/acsenergylett.8b00696.

38 O. E. Everett, P. C. Zonetti, O. C. Alves, R. R. de Avillez and L. G. Appel, The role of oxygen vacancies in the CO_2 methanation employing Ni/ZrO_2 doped with Ca, *Int. J. Hydrogen Energy*, 2020, **45**, 6352–6359, DOI: 10.1016/j.ijhydene.2019.12.140.

39 Y. Yu, *et al.*, Influence of Calcination Temperature on Activity and Selectivity of Ni–CeO_2 and Ni–$Ce_{0.8}Zr_{0.2}O_2$ Catalysts for CO_2 Methanation, *Top. Catal.*, 2018, **61**, 1514–1527, DOI: 10.1007/s11244-018-1010-6.

40 F. Azzolina-Jury and F. Thibault-Starzyk, Mechanism of Low Pressure Plasma-Assisted CO2 Hydrogenation Over Ni-USY by Microsecond Time-resolved FTIR Spectroscopy, *Top. Catal.*, 2017, **60**, 1709–1721, DOI: 10.1007/s11244-017-0849-2.

41 R. Dębek, F. Azzolina-Jury, A. Travert, F. Maugé and F. Thibault-Starzyk, Low-pressure glow discharge plasma-assisted catalytic CO2 hydrogenation—The effect of metal oxide support on the performance of the Ni-based catalyst, *Catal. Today*, 2019, **337**, 182–194, DOI: 10.1016/j.cattod.2019.03.039.

42 A. Parastaev, W. F. L. M. Hoeben, B. E. J. M. van Heesch, N. Kosinov and E. J. M. Hensen, Temperature-programmed plasma surface reaction: An approach to determine plasma-catalytic performance, *Appl. Catal., B*, 2018, **239**, 168–177, DOI: 10.1016/j.apcatb.2018.08.011.

43 F. Azzolina-Jury and F. Thibault-Starzyk, Mechanism of Low Pressure Plasma-Assisted CO2 Hydrogenation Over Ni-USY by Microsecond Time-resolved FTIR Spectroscopy, *Top. Catal.*, 2017, **60**, 1709–1721, DOI: 10.1007/s11244-017-0849-2.

44 H. Chen, *et al.*, Coupling non-thermal plasma with Ni catalysts supported on BETA zeolite for catalytic CO2 methanation, *Catal. Sci. Technol.*, 2019, **9**, 4135–4145, DOI: 10.1039/C9CY00590K.

45 H. Sun, *et al.*, Ru/CeO2 catalysts with enriched oxygen vacancies by plasma treatment for efficient CO2 methanation, *Fuel*, 2025, **381**, 133413, DOI: 10.1016/j.fuel.2024.133413.

46 Y. Huang, *et al.*, Plasma-induced Mo-doped Co_3O_4 with enriched oxygen vacancies for electrocatalytic oxygen evolution in water splitting, *Carbon Energy*, 2023, **5**, 279, DOI: 10.1002/cey2.279.

47 Y.-S. Huang, *et al.*, Enhancing photocatalytic properties of continuous few-layer MoS_2 thin films for hydrogen production by water splitting through defect engineering with Ar plasma treatment, *Nano Energy*, 2023, **109**, 108295, DOI: 10.1016/j.nanoen.2023.108295.